iScience

CellPress
OPEN ACCESS

Article

PPARγ and C/EBPα response to acute cold stress in brown adipose tissue

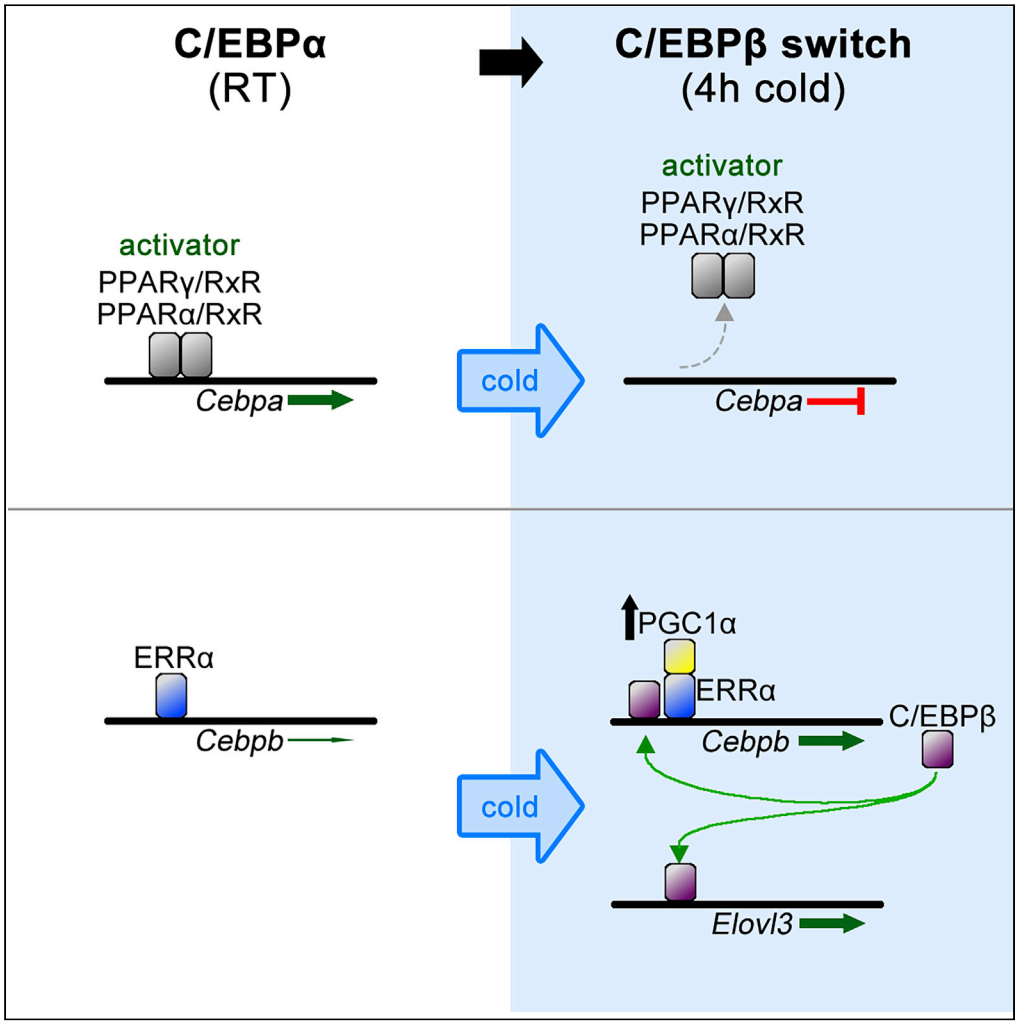

Kin H. Lau, Althea N. Waldhart, Holly Dykstra, Tracey Avequin, Ning Wu

ning@omnispacemail.com

Highlights

Acute cold stress leads to a C/EBPα-to-C/EBPβ switch in BAT

Cold induces dissociation of PPARγ and PPARα from DNA in BAT in a site-specific manner

Dissociation of PPARγ from *Cebpa* enhancer regions is regulated by diet

PGC1α associates with ERRα instead of PPARs after cold stress in BAT

Lau et al., iScience *26*, 105848
January 20, 2023
https://doi.org/10.1016/j.isci.2022.105848

iScience

CellPress
OPEN ACCESS

Article

PPARγ and C/EBPα response to acute cold stress in brown adipose tissue

Kin H. Lau,[1] Althea N. Waldhart,[1] Holly Dykstra,[1] Tracey Avequin,[1] and Ning Wu[1,2,*]

SUMMARY

Brown adipose tissue (BAT) has the ability to burn calories as heat. Utilizing BAT thermogenesis is thus an attractive way to combat obesity. However, the transcriptional network resulting in the lipid synthesis to oxidation shift during thermogenesis is not completely understood. Here, we report the regulation of two master regulators of adipogenesis, peroxisome proliferator-activated receptor gamma (PPARγ) and CCAAT/enhancer-binding protein alpha (C/EBPα), during acute cold stress in BAT. We found PPARγ dissociates from DNA in a fifth of its binding sites and these include *Cebpa* enhancers, leading to decreased C/EBPα expression. This dissociation requires PPARγ binding to activating ligands and is thus modulated by diet. Meanwhile, PPARα also detaches from DNA, and co-activator PGC1α associates with ERRα as part of a transcriptional network regulating lipid metabolism. Subsequent global replacement of C/EBPα by C/EBPβ and its associated transcriptional machinery is required for upregulation of structural lipid synthesis despite general upregulation of fatty acid oxidation.

INTRODUCTION

Brown adipose tissue (BAT) is a tissue specialized for thermogenesis. Upon cold stimulation, brown adipocytes catabolize different sources of carbon–carbon bonds, including self-stored fat, to increase heat generation through the mitochondrial proton gradient.[1,2] The importance of BAT in maintaining body temperature in mice and human infants has long been known. Its identification in human adults and its inverse correlation with obesity have renewed interest in understanding BAT biology.[3] Brown adipocytes have high expression of the adipogenesis master transcription factors, PPARγ and C/EBPα, which drive adipocyte characteristics including lipid accumulation.[4] In order to utilize the energy-burning characteristics of brown adipocytes to counter obesity, an understanding of the regulatory mechanisms of these master transcription factors is required. Here, we report that both PPARγ and C/EBPα must be inactivated either at specific DNA sites (former) or globally (latter) for optimal BAT activation. Upon acute cold stress, PPARγ dissociates from DNA at *Cebpa* enhancers, leading to a decrease of C/EBPα at both the mRNA and protein levels. This dissociation can be modulated by diet through the availability of different lipid ligands for PPARγ. In addition, we found that PPARα, a transcription factor that is known to regulate fatty acid oxidation in the liver, also dissociates from DNA at *Cebpa* enhancers on acute cold stress. After acute cold stress, the co-activator PPARγ co-activator 1 α (PGC1α) co-localizes predominantly with ERRα instead of PPARs; however, not all genes with PGC1α bound have increased expression. C/EBPβ expression increases to replace C/EBPα, and this switch is important for cold activation of the fatty acid elongation pathway.

RESULTS

Acute cold stress induces PPARγ DNA binding changes

PPARγ is a master regulator of adipogenesis. Mice without PPARγ do not develop adipose tissue.[5] PPARγ clearly contributes to lipid accumulation in BAT. However, it is not clear what happens to PPARγ regulation in lipogenic pathways in BAT under cold stress when there is a clear need for an increased fatty acid oxidation. We have previously reported that after 4 h of cold stress treatment, triacylglycerol storage in BAT is decreased.[6] In this current study, we investigated PPARγ binding to DNA in BAT under room temperature (RT) conditions and after 4 h cold (4°C) stress using chromatin immunoprecipitation sequencing (ChIP-seq). Because different PPAR isoforms are highly homologous in both ligand binding and DNA binding domains, we tested many commercial antibodies for their specificity toward PPARγ

[1]Van Andel Institute, Grand Rapids, MI 49503, USA

[2]Lead contact

*Correspondence: ning@omnispacemail.com

https://doi.org/10.1016/j.isci.2022.105848

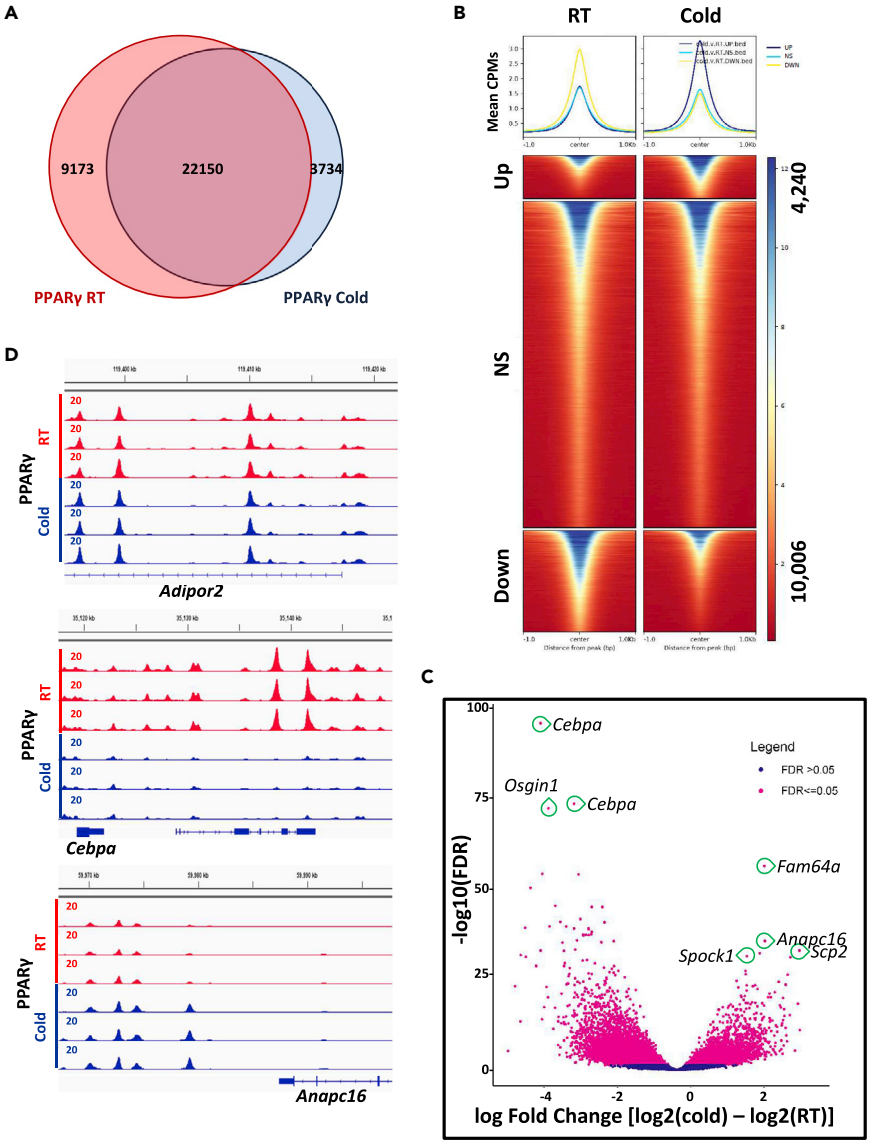

Figure 1. Changes in PPARγ DNA binding after 4 h cold stress as determined by ChIP-seq

(A) Venn diagram showing overlapping PPARγ peaks at RT and after cold stress.

(B) Heatmap showing PPARγ peaks with increased (Up), no significant change (NS), and decreased DNA interaction (Down).

(C) Volcano plot showing PPARγ DNA binding changes from RT conditions to cold, with *Cebpa* enhancers as top decreased interaction sites.

(D) PPARγ DNA binding patterns around *Adipor2*, *Cebpa*, and *anapc16* showing no change, decreased, and increased interaction after cold stress, respectively.

See also Figure S1.

and PPARα (Figure S1A). We overexpressed HA-tagged PPARα and PPARγ in 293T cells, carried out immunoprecipitation with the indicated commercial antibodies, and probed the immunoprecipitates with HA-tag antibody. Two antibodies against the N-terminus of PPARγ were more specific for the γ isoform. We picked the monoclonal N-terminal Cell Signaling Technology antibody for use in ChIP-seq, which was performed in triplicate. Principal component analysis of the ChIP-seq results shows good separation between RT and cold samples (Figure S1B). Counting only the peaks present in all three repeats, we obtained 31,500 peaks for RT and 26,412 peaks for cold stress (Figure S1C), similar to reported values[7] (although Shen et al. used a PPARγ polyclonal antibody that interacted equally well to both γ and α isoforms in our hands (Figure S1A)).

At first glance, there is a good overlap between RT and cold peaks (Figure 1A). However, looking at the peaks more closely, we found PPARγ binding to DNA decreased after cold stress at 10,006 sites, while it showed increased binding at 4,240 sites (Figure 1B). That is, PPARγ lost binding at approximately one-fifth of its binding sites. A volcano plot shows one of the most dramatic sites with decreased PPARγ binding is at *Cebpa* enhancers (Figures 1C and 1D). In comparison, peaks around *Adipor2* did not change, and peaks around *Anapc16* increased (Figure 1D). One very important conclusion from these results is that PPARγ behavior is DNA site-specific, adding another layer of complexity to the function of this nuclear receptor. From adipocyte differentiation studies, it has been found that both PPARγ and C/EBPα are master regulators of adipogenesis and they often bind DNA sites next to each other.[8] Here, PPARγ dissociation from *Cebpa* enhancers may be part of the mechanism leading to a shift in lipid metabolism.

Acute stress induces similar changes in PPARα DNA binding

Because PPARα is also highly expressed in brown adipocytes and binds the same DNA motifs as PPARγ, we wanted to know if PPARα interaction with DNA is also changed by cold stress. In order to ensure we only immunoprecipitated down PPARα, not PPARγ, we made a knock-in (KI) mouse expressing N-terminal HA-tagged PPARα (Figures S2A–S2C) and used HA-tag antibody for ChIP-seq. Western blot showed that HA-PPARα was expressed at the same level as the endogenous PPARα in BAT (Figure 2A). ChIP-seq was done in replicates at RT and triplicates after 4 h cold stress. Results from the two conditions separated out nicely in principal component analysis (Figure S2D). There are 17,811 shared peaks at RT and only 4,079 shared peaks after cold stress (Figure S2E). Most of the PPARα binding sites after cold stress are within the RT sites (Figure 2B). A volcano plot clearly shows decreased PPARα binding to DNA after cold stress (Figure 2C), and *Cebpa* enhancers again have the most significant decrease, just as for PPARγ (Figure 2D).

Comparing PPARγ and PPARα binding sites, we found they mostly overlap at both RT and cold temperature, with a smaller number of peaks identified for PPARα (Figure 2E). Immunohistochemistry (IHC) staining showed that HA-PPARα was expressed in fewer cells than PPARγ (Figure 2F). Quantification of the staining showed HA-PPARα expression in ~60% of BAT nuclei, while PPARγ was expressed in close to 80% of nuclei (Figure 2G). Since the PPARγ antibody used for both ChIP and IHC does not distinguish between γ1 and γ2 splice variants, with γ2 being the variant exclusive for adipocytes, both PPARγ ChIP-seq and IHC results contain population of cells other than brown adipocytes. This may contribute to the larger number of PPARγ peaks compared to PPARα peaks. It is likely that PPARα behavior more closely reflects what happens in brown adipocytes alone, while the PPARγ ChIP-seq results are a composite of what happens in brown adipocytes as well as other cell types such as immune cells. We did not detect any change in PPARα protein levels by Western blot (Figure S2F) after cold stress, but we did detect a decrease in *Ppara* mRNA after cold stress (Figure S2G). It thus appears that in response to cold, BAT reduces PPARα activity through both dissociation of the nuclear receptor from DNA and through the reduction of PPARα mRNA levels.

As shown by volcano plots, both nuclear receptors share similar changes in DNA interactions after cold stress, such as decreased binding around *Cebpa* and *Osgin1* and increased binding around *Fam64a*. We verified this trend globally by taking PPARα sites with significant differential binding after cold stress and examining PPARγ binding at these sites. As heatmaps show, PPARγ binding correlated with that of PPARα (Figure 2H). PPARα-binding DNA sites that showed no significant change in PPARα binding after cold stress also showed no obvious change in PPARγ binding after cold stress (middle block), while DNA sites with decreased binding of PPARα after cold stress also showed decreased PPARγ binding after cold stress (bottom block). Overall, cold stress induces a major trend of decreased PPARα DNA interaction, just as for PPARγ. Therefore, PPARα is likely not a major player in upregulating fatty acid oxidation in BAT in the context of cold stress.

PGC1α interacts with ERRα

Because PPARα is known to upregulate fatty acid oxidation in liver in response to fasting, we assumed it likely also regulates fatty acid oxidation in BAT during cold stress. It was therefore a surprise to find its dissociation from DNA at the same time that brown adipocytes increase fatty acid oxidation. To further investigate this, we wanted to look at PGC1α, which is known to be upregulated by cold stress in BAT[9,10] and regulates fatty acid metabolism via a number of transcription factors including PPARγ and PPARα.[11] In order to carry out ChIP-seq, we made a C-terminal HisHA-tagged PGC1α KI mouse (Figures S3A–S3C). The tagged protein expressed at the same level as the endogenous protein at RT and was induced similarly by cold stress (Figure 3A). IHC showed tagged PGC1α expression in brown

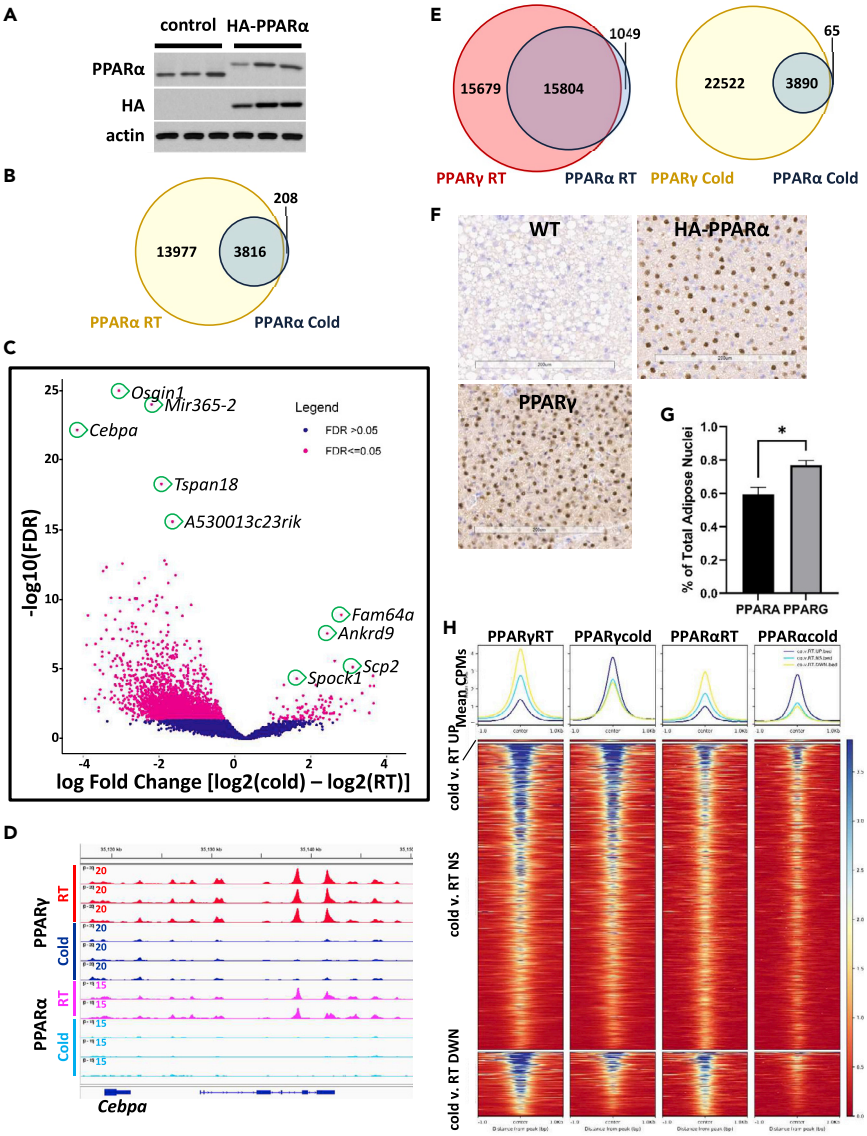

Figure 2. Changes in PPARα DNA binding after 4 h cold stress as determined by ChIP-seq

(A) Western blot comparing endogenous PPARα and HA-PPARα KI expression in BAT at RT.

(B) Venn diagram showing the number of overlapping peaks between the two temperatures.

(C) Volcano plot showing top changes in PPARα DNA binding from RT conditions to cold.

(D) Comparison of PPARγ and PPARα DNA-binding patterns at *Cebpa* enhancers.

(E) Venn diagram comparing the number of PPARγ and PPARα peaks at either RT or after cold stress.

(F) IHC and (G) quantification showing that PPARγ is expressed in more nuclei than PPARα in BAT (mean ± SD).

(H) Global analysis of PPARγ binding status at PPARα-binding sites. The cold-stress-induced decrease in PPARα binding is associated with decreased PPARγ binding at the same DNA sites.

See also Figure S2.

adipocytes, similar to PPARα (Figure 3B). We performed ChIP-seq of PGC1α using HA-tag antibody after 4 h cold stress and identified 1613 peaks that were shared among the triplicates (Figure S3D). Most of the PGC1α peaks were located close to genes, with only about 23% located in distal intergenic regions (Figure S3E). Homer transcription factor motif analysis of the binding sites shows the top motif is estrogen-related receptor beta (ERRβ), which shares the same motif as ERRα and ERRγ (Figure 3C). ERRα is the major isoform in BAT and is known to bind PGC1α in activation of mitochondrial biogenesis,[12,13] which is essential for BAT thermogenesis.[14,15] We carried out ERRα ChIP-seq at RT and after cold stress (Figure S3F) and found that most of the PGC1α binding sites indeed overlapped with ERRα binding sites after cold stress

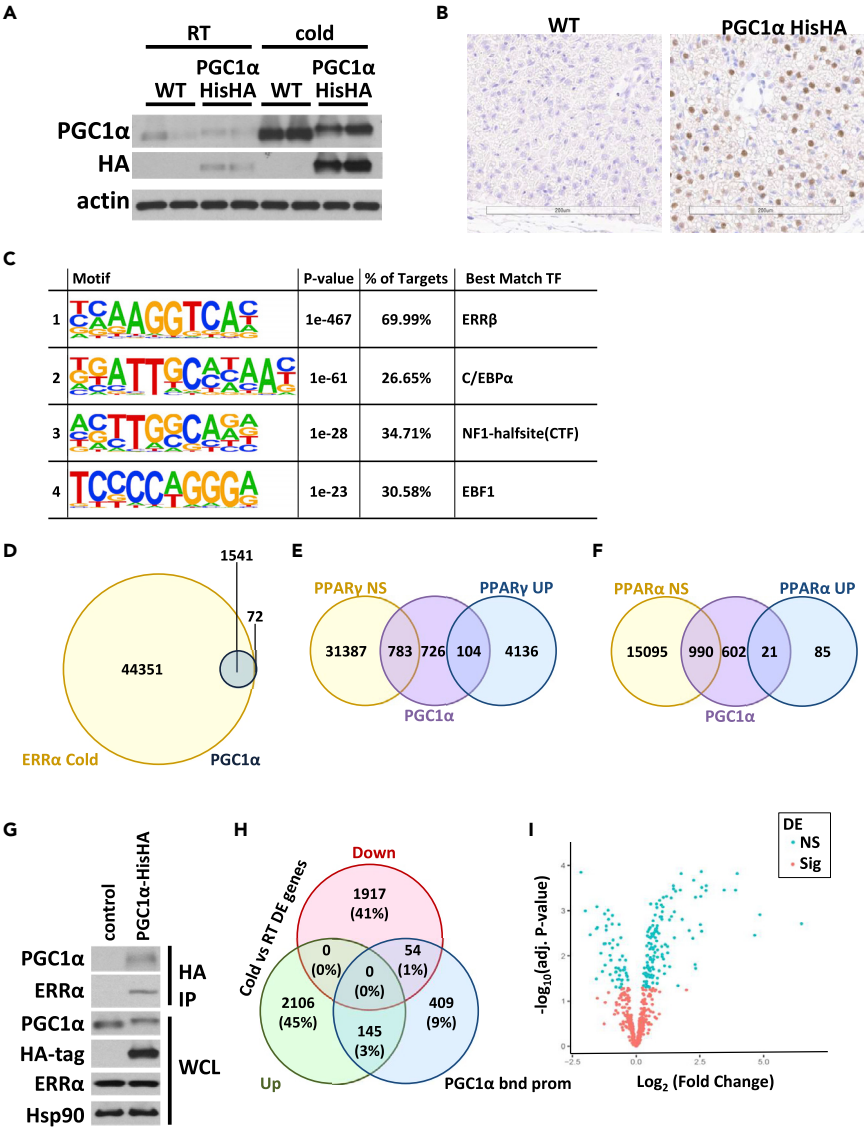

Figure 3. PGC1α ChIP-seq after 4 h cold stress

(A) Western blot showing similar expression levels of endogenous PGC1α and PGC1α-HisHA in BAT before and after 4 h cold stress.

(B) IHC showing PGC1α-HisHA nuclear localization after cold stress.

(C) Homer transcription factor motif analysis of PGC1α peaks.

(D) Venn diagram showing the shared peaks between PGC1α and ERRα after cold stress. Peaks are considered shared if they have greater than 300 bp overlap.

(E) Venn diagram showing the shared peaks between PGC1α and PPARγ peaks that are either not changed (NS) or show increased DNA binding (UP) after cold stress, using the same parameters as in (D).

(F) Same as (E) for PPARα.

(G) Western blot showing PGC1α-HisHA can immunoprecipitate ERRα in BAT after cold stress.

(H) Venn diagram showing overlap between genes with PGC1α bound at the promoter and differentially expressed genes after cold stress.

(I) Cold vs. RT differentially expressed genes with PGC1α bound at the promoter. See also Figure S3 and Table S1. Expression level comparison of genes with PGC1α bound at the promoter before and after cold stress.

(Figure 3D). In contrast, we also compared PPARγ and PPARα binding sites that did not have cold-induced DNA dissociation with PGC1α-binding sites, and we found less overlap (Figures 3E and 3F). In addition, we were able to co-immunoprecipitate ERRα with PGC1α in cold-activated BAT, showing close interaction of

the two proteins (Figure 3G). Therefore, the primary transcription factor interacting with PGC1α in the context of acute brown adipocyte cold stress is ERRα.

As pointed out by Chang et al., we also noticed that not all genes with PGC1α bound were activated.[10] We therefore took genes with PGC1α bound at their promoters and compared them with the gene expression information from our previous mRNAseq data (Table S1).[6] Among genes with PGC1α bound at the promoter, more genes showed increased than decreased expression, although the majority had no expression difference (Figure 3H). This can also be visualized in a volcano plot to show the extent of log-fold changes of gene expression levels with PGC1α bound at promoters (Figure 3I). Because *ppargc1a* (PGC1α) transcription was still being upregulated at the end of 4 h cold stress (Figure S3G), it could be that PGC1α is posed for long-term BAT activation.

C/EBPα to C/EBPβ switch in the BAT response to cold

C/EBPα regulates adipogenesis along with PPARγ, but not in the absence of PPARγ.[16] These two transcription factors bind to DNA sites close to each other.[8] Because we see such a dramatic decrease of PPARγ and PPARα binding to *Cebpa* enhancer sites after cold stress, we wanted to know if C/EBPα expression is affected. Indeed, we found that both C/EBPα mRNA and protein levels decrease as soon as cold stress starts (Figures 4A–4C). At the same time, we found that C/EBPβ is dramatically upregulated at both the mRNA and protein levels (Figures 4B and 4C). Thus, there is a clear switch from C/EBPα to C/EBPβ expression induced by cold stress.

To understand the purpose of this switch, we wanted to know if different C/EBP isoforms bind at different DNA sites. The C/EBP family of proteins has C-terminal leucine zipper DNA binding domains highly homologous to each other, while the N-terminal regulatory domains contain unstructured sequences that vary from each other.[17] In order to clearly differentiate one from another (without running into antibody cross-reaction issues), we constructed HA-tag KI animals. Both C/EBPα and C/EBPβ have long and short isoforms (p42 and p30 for C/EBPα; Lap* and Lap as the long isoforms and Lip as the short isoform for C/EBPβ) due to different translational start sites. There are reports that the shorter isoform of C/EBPβ can act as a negative regulator of the longer isoforms; however, the details are not yet clear.[18] Western blotting showed the disappearance of both translational isoforms of C/EBPα and a dramatic increase of the longer C/EBPβ isoforms after cold stress (Figure 4B); therefore, we tagged both proteins at the N-terminus so that only the longest isoforms will be tagged for both proteins (Figures S4A–S4D). For C/EBPα, the HA-tagged protein was expressed at a slightly lower level than the endogenous protein, but its expression decreased in the same way after cold stress (Figure 4D). For C/EBPβ, tagging seemed to disrupt the translational start site regulation and created multiple C/EBPβ species including Lap* and a higher molecular weight species which was HA-tagged (Figure 4E). At the same time, the expression level of Lap was decreased. To verify the location of the HA-tagged proteins, IHC was used and showed that that the longer isoforms of both C/EBPs were predominantly expressed in brown adipocyte nuclei in BAT (Figure S4E).

With these KI mice, we carried out ChIP-seq experiments with C/EBPα at RT and C/EBPβ after 4 h cold stress. By merging peaks across replicates, we obtained 18,205 peaks for C/EBPα and 25,429 peaks for C/EBPβ (Figures S4F and S4G), and 15,881 of these overlapped (Figure 4F). Furthermore, a heatmap of read coverage at these peaks showed higher read abundance at peaks shared by both transcription factors than at those detected for only either C/EBPα or C/EBPβ, suggesting that the shared peaks are the most strongly bound sites for both transcription factors (Figure 4G). This analysis indicates that sites bound by C/EBPα at RT are replaced by C/EBPβ after cold stress, i.e., they control the same set of genes.

While the decrease in *Cebpa* mRNA can be explained by PPARγ and PPARα dissociation from its enhancers, we wanted to know what drives the increase in *Cebpb* mRNA after cold stress. From ChIP-seq data, we found that all transcription factors investigated here bind to promoter and enhancer regions around *Cebpb* (Figure S4H). Even though there were some decrease of PPARγ and PPARα binding, it was not to the same degree as around *Cebpa*. In addition, C/EBPβ can potentially drive its own expression after cold stress. Furthermore, there is strong binding of ERRα/PGC1α close to the *Cebpb* promoter as well. Therefore, it is likely that cold-induced upregulation of *Cebpb* is due to C/EBPβ-positive feedback and ERRα/PGC1α.

Because PPARγ and C/EBPα often bind to sites that are close to each other, we wondered if degradation of C/EBPα protein causes PPARγ to dissociate from DNA. We examined the PPARγ and C/EBPα peaks, allowing a maximum gap of 1,000 bp between a PPARγ peak and a C/EBPα peak for "overlaps." Then we plotted

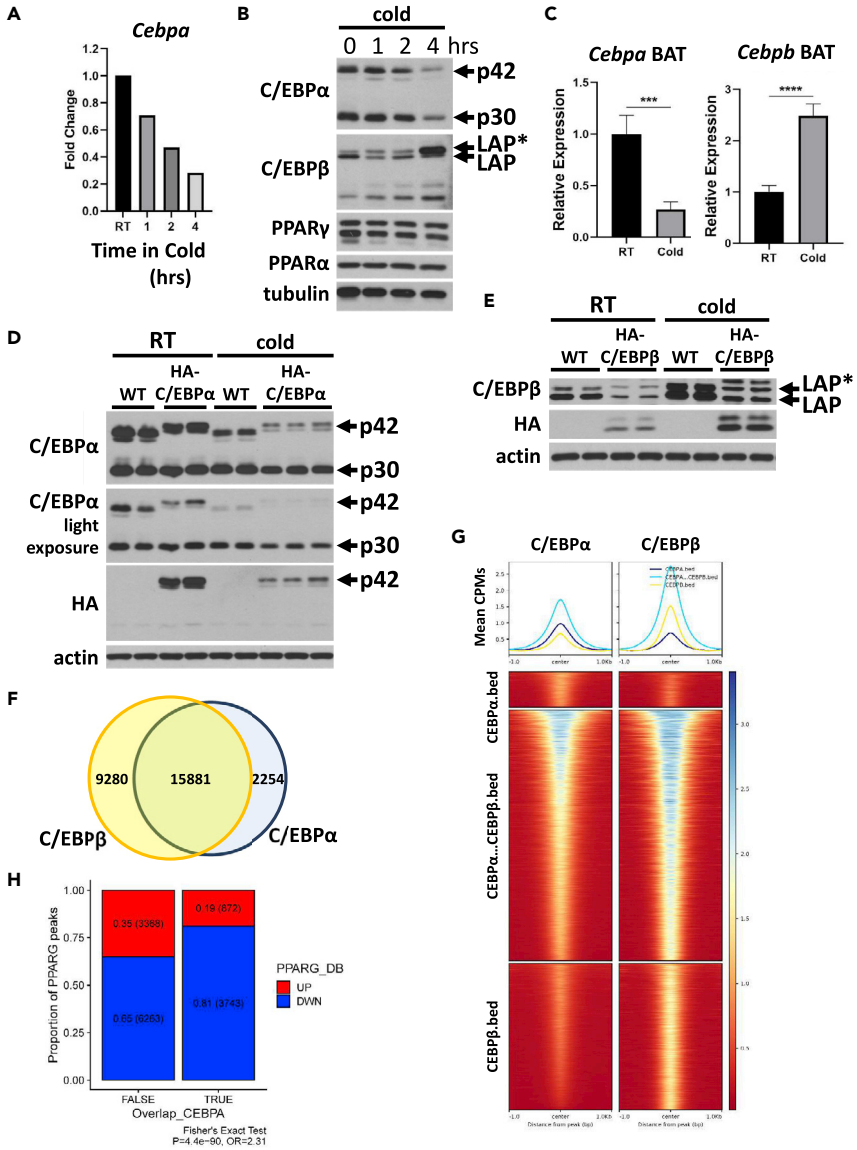

Figure 4. C/EBPβ replaces C/EBPα after cold stress

(A) *Cebpa* mRNA levels as measured by qPCR in a time course of BAT cold stress showing immediate decrease of *Cebpa* mRNA as soon as cold stress starts.

(B) Western blot showing various protein levels in a time course of BAT cold stress.

(C) qPCR quantification of decreased *Cebpa* mRNA and increased *Cebpb* mRNA after 4 h cold stress in BAT (mean ± SD, n = 4).

(D) Western blot showing protein levels of WT and HA-tagged C/EBPα in BAT before and after 4 h cold stress.

(E) Western blot showing protein levels of WT and HA-tagged C/EBPβ in BAT before and after 4 h cold stress.

(F) Venn diagram showing the number of shared ChIP-seq peaks between C/EBPα at RT and C/EBPβ after 4 h cold stress.

(G) Heatmap showing ChIP-seq peaks shared by C/EBPα at RT and C/EBPβ after 4 h cold stress are stronger binding sites for both transcription factors. (CPM = counts per million).

(H) PPARγ peaks are divided into two groups: FALSE = no overlap with C/EBPα and TRUE = within 1,000 bp from a C/EBPα peak. A higher proportion of PPARγ peaks in the TRUE group lose interaction with DNA after cold stress than in the FALSE group. See also Figure S4.

the proportions of PPARγ up and down peaks for those that overlap with C/EBPα peaks (Figure 4H right, "True") and those that do not overlap with C/EBPα peaks (Figure 4H left, "False"). For the PPARγ peaks that do not overlap with C/EBPα peaks, 65% of these show decreased binding with DNA after cold stress. For

the PPARγ peaks that do overlap with C/EBPα peaks, 81% of these show decreased binding with DNA after cold stress. Similar results were obtained if PPARγ and C/EBPα peaks were required to overlap at least 1 bp (data not shown). The increased percentage of PPARγ peaks losing DNA binding in the vicinity of C/EBPα sites may indicate a trend of PPARγ and C/EBPα being regulated in the same way, but it does not conclusively show that C/EBPα protein degradation is the cause of PPARγ dissociation from DNA. Therefore, even though there is a global switch from C/EBPα expression to C/EBPβ expression after cold stress, this switch is not fully responsible for PPARγ dissociating from DNA after cold stress. Given the data so far, it is likely that PPARγ and PPARα dissociation from *Cebpa* enhancer is the cause of *Cebpa* mRNA decrease and subsequent C/EBPα replacement by C/EBPβ.

C/EBPβ activation is necessary for optimal BAT thermogenesis

The switch from C/EBPα expression to C/EBPβ expression must have a functional reason. Because both bind the same DNA sites, we hypothesize that the N-terminal unstructured regions of these transcription factors recruit different transcriptional co-activator complexes. We already know from ChIP-seq peak alignments that PGC1α may not be the only co-activator for C/EBPβ because only a very small fraction of C/EBPβ sites have PGC1α bound (Figure 5A). Another co-activator, nuclear receptor co-activator 1 (NCOA1), was reported to coordinate the activity of C/EBPα in hepatic glucose production.[19] We carried out HA-tag immunoprecipitations of HA-C/EBPα BAT at RT and HA-C/EBPβ BAT after cold stress and then probed the immunoprecipitates for NCOA1 by Western blot (Figure 5B). Unlike what happens in the liver, we found interaction of NCOA1 with C/EBPβ but not with C/EBPα. This piece of evidence indicates that C/EBPα and C/EBPβ form different transcriptional complexes. The isoform switch changes the potential regulatory mechanisms of the downstream genes under C/EBP control. Similar to the PPARγ DNA site-dependent behavior, C/EBPβ association with NCOA1 can also be site-specific; therefore, not all C/EBPβ-bound sites necessarily lead to gene expression changes.

In an attempt to identify the genes regulated by the C/EBPα-to-β switch, we generated adipose tissue-specific knockout (KO) of *Cebpb* (AKO$^{\beta}$) using AdiQ-Cre (JAX 028020) and *Cebpb* flox/flox (JAX 032282) mice. Then we carried out mRNA-Seq of littermate-matched WT/AKO$^{\beta}$ mice at RT and after 4 h cold stress. In comparing differential gene expressions, we found a large difference between RT and cold, as expected (Figures S5A and S5B). However, we did not find much difference in gene expression between WT and AKO$^{\beta}$ at either temperature (Figures S5C and S5D). It turned out that while C/EBPβ expression was efficiently knocked out both before and after cold stress, C/EBPα protein levels were upregulated in AKO$^{\beta}$ (Figure 5C). This compensation happens at the C/EBPα protein level, not at the *Cebpa* mRNA level (Figure 5D). This complicates the interpretation of the mRNA-Seq data and means that many genes affected by the C/EBPα-to-β switch might potentially go undetected in our AKO$^{\beta}$ mice.

To reduce the complications resulting from C/EBPα compensation in AKO$^{\beta}$, we decided to focus on genes whose expression was acutely changed by cold stress. We identified genes whose expression was either increased or decreased by cold stress in WT, but with blunted change in AKO$^{\beta}$ (Table S2). Two genes in the fatty acid elongation pathway, *Elovl3* and *Hacd2*, stood out as C/EBPβ targets (Figures 5E and 5F). In the absence of C/EBPβ, upregulation of both genes by cold stress is blunted. Elovl3 is the first and also the rate-limiting step of each round of fatty acid elongation. We have previously reported that the upregulation of *Elovl3* during BAT cold stress is important for mitochondrial function.[6] *Elovl3* transcription is regulated by three upstream enhancer regions and both PPARγ and PPARα regulate *Elovl3* expression in BAT.[20,21] ChIP-seq data not only showed C/EBPα and C/EBPβ binding at RT and after cold stress, respectively, to the enhancer closest to *Elovl3* but also showed increased PPARγ binding at this enhancer after cold stress (Figure 5G). Clearly, C/EBPβ and PPARγ both play a role in *Elovl3* upregulation by cold stress. At the same time, there seems to be a trend of increased PPARα binding at the same enhancer after cold. Given that the PPARα agonist fenofibrate can also activate *Elovl3* in BAT,[7] it is likely PPARα plays a role as well. However, whether a similar type of co-operativity exists for *Hacd2* is not clear because *Hacd2* enhancers have not been clearly defined. Given the importance of Elovl3 activity to BAT thermogenesis,[22,23] we can conclude that C/EBPβ is required for optimal BAT function.

Comparison of gene expression levels showed that *Elovl6* is the most abundant elongase, while *Elovl3* is the only elongase with a response to cold stress in BAT (Figure S5E). Elovl6 catalyzes the formation of C18:0-CoA from C16:0-CoA, the product of fatty acid synthetase, and is an important player in *de novo* lipid synthesis. One conclusion on metabolism we can draw from *Elovl3* regulation is that cells can differentiate

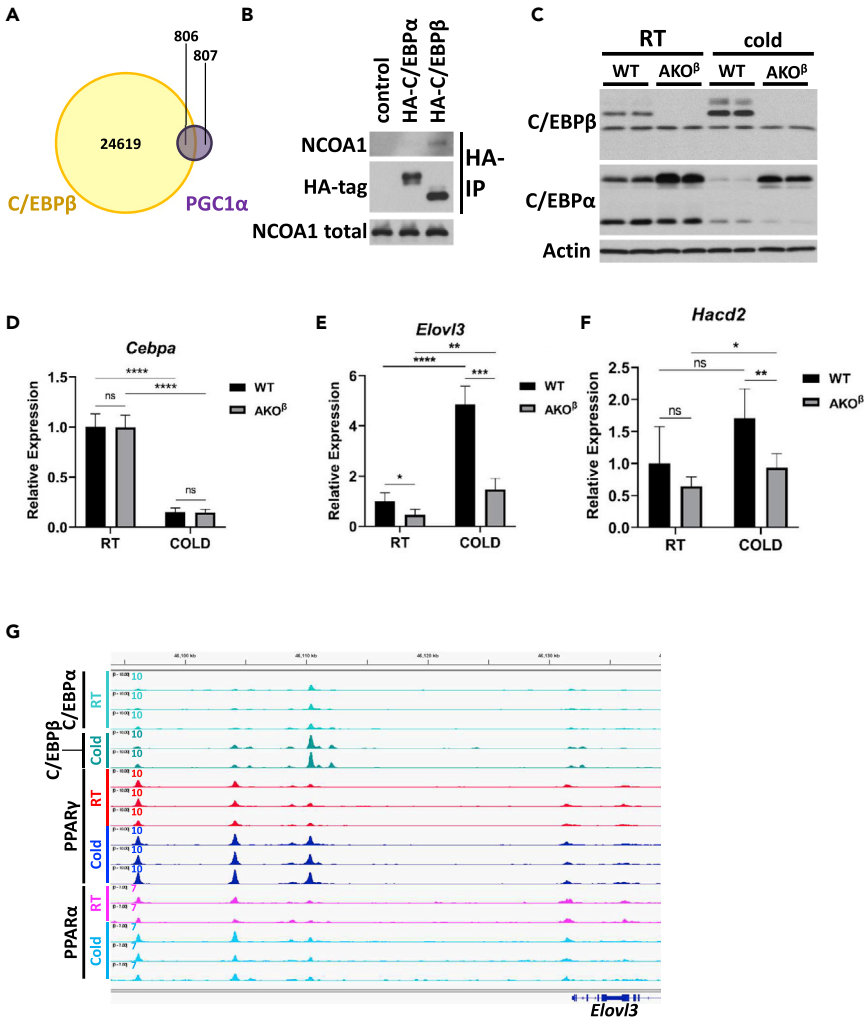

Figure 5. C/EBPβ is necessary for optimal cold stress response in BAT

(A) Overlapping of PGC1α and C/EBPβ peaks after cold stress.

(B) Immunoprecipitation with HA-tag antibody and Western blot experiment showing selective NCOA1 interaction with C/EBPβ.

(C) Western blot of C/EBPβ and C/EBPα protein expression in WT and AKO$^{\beta}$ BAT.

(D) qPCR of *Cebpa* mRNA levels in WT and AKO$^{\beta}$ BAT (mean ± SD, n = 5).

(E) qPCR quantification of *Elovl3* and (F) *Hacd2* mRNA in WT and AKO$^{\beta}$ BAT (mean ± SD, n = 5).

(G) ChIP-seq peak distribution around the *Elovl3* enhancer region. See also Figure S5 and Table S2. Cold induced differentially expressed genes in WT that had reduced change in AKOβ.

different types of fatty acids and regulate their fate differently. While much of the stored fatty acids are used for oxidation to generate heat, long-chain polyunsaturated fatty acids are made to maintain the fluidity needed for structural membranes. The transcriptional control required for differential regulation is however very complex, as illustrated here.

C/EBPα to C/EBPβ switch is diet-dependent

Previously, we studied the effects of excess glucose on BAT mitochondrial function using the *Txnip* KO model.[6] TXNIP is an α-arrestin adaptor that facilitates the endocytosis of glucose transporters.[24–26] In its absence, basal glucose uptake into cells increases. *De novo* lipid synthesis from the excess glucose increased the content of short and more saturated acyl-chains both in the stored triacylglycerides and in structural phospholipids. This lipid composition change led to reduced fluidity of mitochondrial membranes and compromised the mitochondrial ability to increase metabolic flux during cold stress. We noticed that the inhibition of *Cebpa* expression by

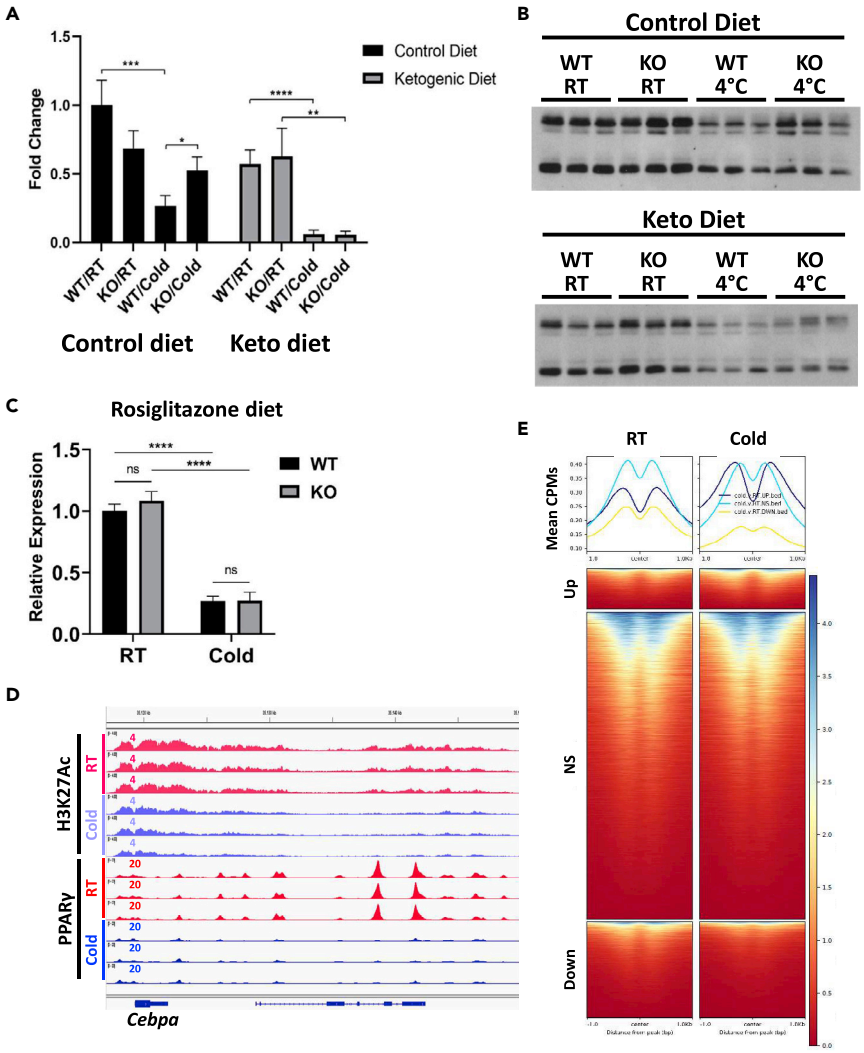

Figure 6. *Cebpa* expression is diet dependent

(A) qPCR results showing **that in TXNIP KO BAT, the cold-stress-induced decrease in Cebpa mRNA levels occurs to a lesser extent than in WT BAT** on control diet and this difference is eliminated by a ketogenic diet (mean ± SD, n = 4).

(B) Western blot showing the same results as in (A) on C/EBPα protein levels.

(C) qPCR showing that a diet with rosiglitazone reduces the difference between TXNIP WT and KO BAT in *Cebpa* expression after cold just like the ketogenic diet (mean ± SD, n = 4).

(D) ChIP-seq peaks showing decreased H3K27Ac mark around *Cebpa* after cold stress along with decreased PPARγ binding.

(E) Heatmap showing that global changes in PPARγ DNA interactions induced by cold stress are correlated with changes in H3K27Ac.

See also Figure S6.

cold was blunted in *Txnip* KO (Figure 6A). This was also reflected at the protein level (Figure 6B). When the excess glucose uptake phenotype in *Txnip* KO mice was rescued with a ketogenic diet,[6] *Cebpa* and C/EBPα behavior was also rescued (Figures 6A and 6B). This means that *Cebpa* is either directly regulated by glucose or indirectly regulated through glucose's effect on lipid composition.

Because PPARα and γ both bind to *Cebpa* enhancers, and both nuclear receptors use lipids as ligands, we wondered if lipid composition affects *Cebpa* expression driven by PPARs. As an example, we focused on PPARγ. Given the ketogenic diet result, we hypothesized a PPARγ agonist such as rosiglitazone would promote the repression of *Cebpa* in *Txnip* KO mice to the same levels seen in WT mice after cold stress. That was indeed the case (Figure 6C); we saw equally suppressed *Cebpa* expression in both WT and KO after

feeding them a rosiglitazone-containing diet for 2 weeks. This indicates that it is the activated form of PPARγ, which dissociates from DNA leading to decreased transcription, quite the opposite of the conventional wisdom that agonists only activate PPARγ to upregulate transcription. Many types of lipids can act as PPARγ endogenous ligands, including medium chain fatty acids (MCFA) as low affinity ligands.[27] These fatty acids have lower affinities than longer polyunsaturated fatty acids and artificial agonists because they generally occupy less space in the ligand binding site.[28] Our results suggest PPARγ function is affected by the type of endogenous ligand it is associated with. If more MCFA binding to PPARγ in TXNIP KO leads to less responsive PPARγ in turning off *Cebpa* transcription, then C/EBPβ replacement of C/EBPα on DNA would be slower, followed by a decrease in *Elovl3* upregulation driven by C/EBPβ.

Because both PPARγ and PPARα show detachment from the DNA around *Cebpa* enhancers after cold stress, we wanted to know if chromatin structural change is the cause of this detachment by using histone H3 lysine 27 acetylation (H3K27Ac) ChIP-seq. H3K27Ac is a marker for open chromatin around enhancers and promoters. ChIP-seq data indeed showed decreased H3K27Ac mark around *Cebpa* enhancers after cold stress (Figure 6D). More importantly, we found a correlation between decreased PPARγ binding to DNA with a decrease in H3K27Ac globally (Figure 6E). We took upregulated, downregulated, and non-significant PPARγ peaks after cold stress, plotted mean counts per million (CPM) of H3K27Ac signal around the peaks, and found increased H3K27Ac signal for upregulated PPARγ peaks (dark blue line), no change around non-significant peaks (light blue line), and decreased signal around downregulated peaks (yellow line). In other words, there is correlated H3K27Ac signal around PPARγ binding sites. This result suggests PPARγ DNA interaction patterns are associated with H3K27Ac status.

We then performed H3K27Ac ChIP-seq in TXNIP WT/KO littermates to see if there are changes in chromatin structures that can potentially influence PPARs behavior. While cold stress induced many H3K27Ac changes (Figure S6A), there are very few significant changes between TXNIP WT and KO at either temperature (Figure S6B). These significant changes did not include *Cebpa* enhancers. This means H3K27Ac histone modification does not play a significant role in TXNIP-dependent PPARγ-*Cebpa* behavior. Therefore, even though chromatin openness is a good reflection of gene expression in general, it is not likely a causal factor for PPARs detaching around *Cebpa*.

DISCUSSION

Transcriptional regulation is difficult to decipher for many reasons. After all, this ultimate cellular response to the environment has to be sensitive enough to distinguish the smallest differences among similar types of stimulations. Here we focused on the behavior of two adipogenesis master regulators in the acute cold response of BAT. We learned (1) PPARγ and PPARα both dissociate from *Cebpa* enhancers to reduce *Cebpa* transcription while C/EBPα is quickly replaced by C/EBPβ, (2) the transcriptional programming associated with the switch to C/EBPβ is required for proper activation of the fatty acid elongation pathway, (3) excess carbohydrates can influence PPARγ behavior via modulating the available pool of lipid ligands, and (4) PGC1α is predominantly a co-factor for ERRα instead of PPARs in this context.

We started our investigation of PPARγ and C/EBPα because we were interested in how the opposing fatty acid synthesis and oxidation are regulated on BAT activation. Because the mice were maintained at RT, which is below their thermoneutral temperature, BAT had semi-activated metabolic programming for thermogenesis. Yet, there was clear evidence for the inhibition of lipid synthesis within 4 h of cold stress at the mRNA level of key genes such as *Acaca*, which is responsible for producing the starting substrate malonyl-CoA, and *Dgat2*, which is involved in the committed step for triacylglyceride synthesis.[6] However, at the transcriptional level, all transcription factors studied here are involved in altering lipid metabolism as follows: the PPARs site-specific response, the C/EBPs isoform switch, and ERRα association with PGC1α. Data presented here support the complexity of a transcriptional network with many transcription factors working together in a combinatorial way to fine-tune the outcome. Clearly, lipid metabolism involved in BAT thermogenesis cannot be simply lumped into synthesis and oxidation as two opposing processes. An important message from this work is the separate regulation of lipids used for energy and lipids used for structural purposes. Without knowing whether the cold stress will persist, the animal responds with mitobiogenesis, which requires synthesis of phospholipids and long-chain polyunsaturated acyl-chains for structural lipids.

However, we did learn that the PPARs response to cold is DNA site-specific. DNA sites with decreased PPARs binding include *Cebpa* enhancers and sites with increased binding include *elovl3* enhancers. This

observation sheds new lights on PPAR mechanism of action. In the traditional view, PPARs bind to DNA as a heterodimer with retinoic acid receptors (RxRs), and the availability of ligands causes conformational changes such that the heterodimer dissociates from co-repressors and associates with co-activators, which then bring in chromatin modifiers and transcription machinery.[29] However, not all PPARγ/RxR co-repressor complexes can bind DNA.[30,31] Here, we did not investigate PPARs binding to co-repressors, but the data clearly showed that the dissociation of PPARs from DNA can be a way to regulate their activity. In addition, prompt dissociation of PPARs (at least PPARγ) from DNA relies on binding of "activating" ligands. In other words, shutting down PPARs may require them to already be in an active state, as exemplified by *Cebpa* enhancers. Therefore, it is likely that PPARs-DNA dissociation precedes co-repressor binding. What happens to PPAR-ligands association after dissociation from DNA is an intriguing question. However, we do not have clear evidence that an increased association of PPARs with DNA such as *Elovl3* enhancers is also affected by the type of ligands bound. The existence of three different types of PPARs DNA binding response to cold stress indicates that the activity of PPARs encompasses more than just their ligand binding status. It is possible post-translational modification plays a role in site-specific behavior.[32] This location dependency certainly makes prediction of PPARs-controlled gene transcription under different stimulations much more complicated. Further work in clarifying mechanistic details on how PPARγ detaches from DNA in the presence of agonists, and how various types of endogenous ligands affect PPARγ function will be beneficial for treatment of obesity.

Our work did not distinguish between PPARγ2, which is the adipose-specific isoform, and PPARγ1, which is more ubiquitously expressed, including in immune cells. The PPARγ ChIP-seq results also include those from cell types other than brown adipocytes. In addition, we still do not know the functional differences between PPARγ and PPARα in BAT. To compare PPARγ isoforms and PPARα mechanisms of action more specifically in brown adipocytes, single-cell techniques that do not disturb the cellular cold response will be needed. However, with the results here, we can conclude that at least PPARα is not the PGC1α binding partner for upregulating fatty acid oxidation in BAT thermogenesis. To use BAT energy expenditure properties as a treatment for obesity, enhancing PGC1α-ERRα binding may be a viable option.

Limitations of the study

Other than the limitations already mentioned in the text such as increased C/EBPα compensating for the lack of C/EBPβ in the *Cebpb* AKO mice, this study has one other notable limitation. Specifically, adding an HA-tag DNA sequence to *Cebpa* and *Cebpb* after the start codon affected their protein expression compared with the wild-type mice. We do not know if there are any consequences because of these protein expression changes on their DNA binding location distribution, i.e., ChIP-seq results.

STAR★METHODS

Detailed methods are provided in the online version of this paper and include the following:

- KEY RESOURCES TABLE
- RESOURCE AVAILABILITY
  - Lead contact
  - Materials availability
  - Data and code availability
- EXPERIMENTAL MODEL AND SUBJECT DETAILS
- METHOD DETAILS
  - Tagged knock-in mice construction
  - Western blots
  - Histology
  - ChIP-seq
  - Immunoprecipitation
  - mRNAseq and qPCR
  - Bioinformatics: ChIP-seq analysis
  - Bioinformatics: RNA-seq analysis
- QUANTIFICATION AND STATISTICAL ANALYSIS

SUPPLEMENTAL INFORMATION

Supplemental information can be found online at https://doi.org/10.1016/j.isci.2022.105848.

ACKNOWLEDGMENTS

The authors thank the VAI genomics core for all the sequencing support, the VAI histology core for IHC, and the VAI vivarium transgenic core for making the KI mouse lines. N.W. is supported by R01-GM120129.

AUTHOR CONTRIBUTIONS

N.W. conceived the idea and designed and carried out most of the experiments with the help of A.N.W. K.H.L. did all the bioinformatic analysis. T.A. and H.D. did most of the IHC quantification and qPCR analysis.

DECLARATION OF INTERESTS

The authors declare no competing interests.

Received: September 29, 2022
Revised: November 14, 2022
Accepted: December 19, 2022
Published: January 20, 2023

REFERENCES

1. Blondin, D.P., Frisch, F., Phoenix, S., Guérin, B., Turcotte, É.E., Haman, F., Richard, D., and Carpentier, A.C. (2017). Inhibition of intracellular triglyceride lipolysis suppresses cold-induced Brown adipose tissue metabolism and increases shivering in humans. Cell Metab. *25*, 438–447.

2. Weir, G., Ramage, L.E., Akyol, M., Rhodes, J.K., Kyle, C.J., Fletcher, A.M., Craven, T.H., Wakelin, S.J., Drake, A.J., Gregoriades, M.L., et al. (2018). Substantial metabolic activity of human Brown adipose tissue during warm conditions and cold-induced lipolysis of local triglycerides. Cell Metab. *27*, 1348–1355.e4.

3. Betz, M.J., and Enerbäck, S. (2015). Human Brown adipose tissue: what we have learned so far. Diabetes *64*, 2352–2360.

4. Lee, J.E., Schmidt, H., Lai, B., and Ge, K. (2019). Transcriptional and epigenomic regulation of adipogenesis. Mol. Cell. Biol. *39*, e00601-18.

5. Wang, F., Mullican, S.E., DiSpirito, J.R., Peed, L.C., and Lazar, M.A. (2013). Lipoatrophy and severe metabolic disturbance in mice with fat-specific deletion of PPARgamma. Proc. Natl. Acad. Sci. USA *110*, 18656–18661.

6. Waldhart, A.N., Muhire, B., Johnson, B., Pettinga, D., Madaj, Z.B., Wolfrum, E., Dykstra, H., Wegert, V., Pospisilik, J.A., Han, X., and Wu, N. (2021). Excess dietary carbohydrate affects mitochondrial integrity as observed in brown adipose tissue. Cell Rep. *36*, 109488.

7. Shen, Y., Su, Y., Silva, F.J., Weller, A.H., Sostre-Colón, J., Titchenell, P.M., Steger, D.J., Seale, P., and Soccio, R.E. (2020). Shared PPARalpha/gamma target genes regulate Brown adipocyte thermogenic function. Cell Rep. *30*, 3079–3091.e5.

8. Lefterova, M.I., Zhang, Y., Steger, D.J., Schupp, M., Schug, J., Cristancho, A., Feng, D., Zhuo, D., Stoeckert, C.J., Jr., Liu, X.S., and Lazar, M.A. (2008). PPARgamma and C/EBP factors orchestrate adipocyte biology via adjacent binding on a genome-wide scale. Genes Dev. *22*, 2941–2952.

9. Puigserver, P., Wu, Z., Park, C.W., Graves, R., Wright, M., and Spiegelman, B.M. (1998). A cold-inducible coactivator of nuclear receptors linked to adaptive thermogenesis. Cell *92*, 829–839.

10. Chang, J.S., Ghosh, S., Newman, S., and Salbaum, J.M. (2018). A map of the PGC-1alpha- and NT-PGC-1alpha-regulated transcriptional network in brown adipose tissue. Sci. Rep. *8*, 7876.

11. Cheng, C.F., Ku, H.C., and Lin, H. (2018). PGC-1alpha as a pivotal factor in lipid and metabolic regulation. Int. J. Mol. Sci. *19*, 3447.

12. Schreiber, S.N., Emter, R., Hock, M.B., Knutti, D., Cardenas, J., Podvinec, M., Oakeley, E.J., and Kralli, A. (2004). The estrogen-related receptor alpha (ERRalpha) functions in PPARgamma coactivator 1alpha (PGC-1alpha)-induced mitochondrial biogenesis. Proc. Natl. Acad. Sci. USA *101*, 6472–6477.

13. Huss, J.M., Kopp, R.P., and Kelly, D.P. (2002). Peroxisome proliferator-activated receptor coactivator-1alpha (PGC-1alpha) coactivates the cardiac-enriched nuclear receptors estrogen-related receptor-alpha and -gamma. Identification of novel leucine-rich interaction motif within PGC-1alpha. J. Biol. Chem. *277*, 40265–40274.

14. Villena, J.A., Hock, M.B., Chang, W.Y., Barcas, J.E., Giguère, V., and Kralli, A. (2007). Orphan nuclear receptor estrogen-related receptor alpha is essential for adaptive thermogenesis. Proc. Natl. Acad. Sci. USA *104*, 1418–1423.

15. Brown, E.L., Hazen, B.C., Eury, E., Wattez, J.S., Gantner, M.L., Albert, V., Chau, S., Sanchez-Alavez, M., Conti, B., and Kralli, A. (2018). Estrogen-related receptors mediate the adaptive response of Brown adipose tissue to adrenergic stimulation. iScience *2*, 221–237.

16. Rosen, E.D., Hsu, C.H., Wang, X., Sakai, S., Freeman, M.W., Gonzalez, F.J., and Spiegelman, B.M. (2002). C/EBPalpha induces adipogenesis through PPARgamma: a unified pathway. Genes Dev. *16*, 22–26.

17. Tsukada, J., Yoshida, Y., Kominato, Y., and Auron, P.E. (2011). The CCAAT/enhancer (C/EBP) family of basic-leucine zipper (bZIP) transcription factors is a multifaceted highly-regulated system for gene regulation. Cytokine *54*, 6–19.

18. Bégay, V., Baumeier, C., Zimmermann, K., Heuser, A., and Leutz, A. (2018). The C/EBPbeta LIP isoform rescues loss of C/EBPbeta function in the mouse. Sci. Rep. *8*, 8417.

19. Louet, J.F., Chopra, A.R., Sagen, J.V., An, J., York, B., Tannour-Louet, M., Saha, P.K., Stevens, R.D., Wenner, B.R., Ilkayeva, O.R., et al. (2010). The coactivator SRC-1 is an essential coordinator of hepatic glucose production. Cell Metab. *12*, 606–618.

20. Jörgensen, J.A., Zadravec, D., and Jacobsson, A. (2007). Norepinephrine and rosiglitazone synergistically induce Elovl3 expression in brown adipocytes. Am. J. Physiol. Endocrinol. Metab. *293*, E1159–E1168.

21. Jakobsson, A., Jörgensen, J.A., and Jacobsson, A. (2005). Differential regulation of fatty acid elongation enzymes in brown adipocytes implies a unique role for Elovl3 during increased fatty acid oxidation. Am. J. Physiol. Endocrinol. Metab. *289*, E517–E526.

22. Westerberg, R., Månsson, J.E., Golozoubova, V., Shabalina, I.G., Backlund, E.C., Tvrdik, P., Retterstøl, K., Capecchi, M.R., and Jacobsson, A. (2006). ELOVL3 is an important component for early onset of lipid recruitment in brown adipose tissue. J. Biol. Chem. *281*, 4958–4968.

23. Tvrdik, P., Westerberg, R., Silve, S., Asadi, A., Jakobsson, A., Cannon, B., Loison, G., and Jacobsson, A. (2000). Role of a new mammalian gene family in the biosynthesis of very long chain fatty acids and sphingolipids. J. Cell Biol. *149*, 707–718.

24. Wu, N., Zheng, B., Shaywitz, A., Dagon, Y., Tower, C., Bellinger, G., Shen, C.H., Wen, J., Asara, J., McGraw, T.E., et al. (2013). AMPK-dependent degradation of TXNIP upon

energy stress leads to enhanced glucose uptake via GLUT1. Mol. Cell *49*, 1167–1175.

25. Waldhart, A.N., Dykstra, H., Peck, A.S., Boguslawski, E.A., Madaj, Z.B., Wen, J., Veldkamp, K., Hollowell, M., Zheng, B., Cantley, L.C., et al. (2017). Phosphorylation of TXNIP by AKT mediates acute influx of glucose in response to insulin. Cell Rep. *19*, 2005–2013.

26. Parikh, H., Carlsson, E., Chutkow, W.A., Johansson, L.E., Storgaard, H., Poulsen, P., Saxena, R., Ladd, C., Schulze, P.C., Mazzini, M.J., et al. (2007). TXNIP regulates peripheral glucose metabolism in humans. PLoS Med. *4*, e158.

27. Liberato, M.V., Nascimento, A.S., Ayers, S.D., Lin, J.Z., Cvoro, A., Silveira, R.L., Martínez, L., Souza, P.C.T., Saidemberg, D., Deng, T., et al. (2012). Medium chain fatty acids are selective peroxisome proliferator activated receptor (PPAR) gamma activators and pan-PPAR partial agonists. PLoS One *7*, e36297.

28. Shang, J., Brust, R., Mosure, S.A., Bass, J., Munoz-Tello, P., Lin, H., Hughes, T.S., Tang, M., Ge, Q., Kamenekca, T.M., and Kojetin, D.J. (2018). Cooperative cobinding of synthetic and natural ligands to the nuclear receptor PPARgamma. Elife *7*, e43320.

29. Weikum, E.R., Liu, X., and Ortlund, E.A. (2018). The nuclear receptor superfamily: a structural perspective. Protein Sci. *27*, 1876–1892.

30. Zamir, I., Zhang, J., and Lazar, M.A. (1997). Stoichiometric and steric principles governing repression by nuclear hormone receptors. Genes Dev. *11*, 835–846.

31. Guo, C., Li, Y., Gow, C.H., Wong, M., Zha, J., Yan, C., Liu, H., Wang, Y., Burris, T.P., and Zhang, J. (2015). The optimal corepressor function of nuclear receptor corepressor (NCoR) for peroxisome proliferator-activated receptor gamma requires G protein pathway suppressor 2. J. Biol. Chem. *290*, 3666–3679.

32. Brunmeir, R., and Xu, F. (2018). Functional regulation of PPARs through post-translational modifications. Int. J. Mol. Sci. *19*, 1738.

33. Li, H. (2013). Aligning sequence reads, clone sequences and assembly contigs with BWA-MEM. Preprint at ArXiv. https://doi.org/10.48550/arXiv.1303.3997.

34. Faust, G.G., and Hall, I.M. (2014). SAMBLASTER: fast duplicate marking and structural variant read extraction. Bioinformatics *30*, 2503–2505.

35. Li, H., Handsaker, B., Wysoker, A., Fennell, T., Ruan, J., Homer, N., Marth, G., Abecasis, G., and Durbin, R.; 1000 Genome Project Data Processing Subgroup (2009). The sequence alignment/map format and SAMtools. Bioinformatics *25*, 2078–2079.

36. Zhang, Y., Liu, T., Meyer, C.A., Eeckhoute, J., Johnson, D.S., Bernstein, B.E., Nusbaum, C., Myers, R.M., Brown, M., Li, W., and Liu, X.S. (2008). Model-based analysis of ChIP-seq (MACS). Genome Biol. *9*, R137.

37. Quinlan, A.R., and Hall, I.M. (2010). BEDTools: a flexible suite of utilities for comparing genomic features. Bioinformatics *26*, 841–842.

38. Ramírez, F., Ryan, D.P., Grüning, B., Bhardwaj, V., Kilpert, F., Richter, A.S., Heyne, S., Dündar, F., and Manke, T. (2016). deepTools2: a next generation web server for deep-sequencing data analysis. Nucleic Acids Res. *44*, W160–W165.

39. Zerbino, D.R., Johnson, N., Juettemann, T., Wilder, S.P., and Flicek, P. (2014). WiggleTools: parallel processing of large collections of genome-wide datasets for visualization and statistical analysis. Bioinformatics *30*, 1008–1009.

40. Kent, W.J., Zweig, A.S., Barber, G., Hinrichs, A.S., and Karolchik, D. (2010). BigWig and BigBed: enabling browsing of large distributed datasets. Bioinformatics *26*, 2204–2207.

41. Ross-Innes, C.S., Stark, R., Teschendorff, A.E., Holmes, K.A., Ali, H.R., Dunning, M.J., Brown, G.D., Gojis, O., Ellis, I.O., Green, A.R., et al. (2012). Differential oestrogen receptor binding is associated with clinical outcome in breast cancer. Nature *481*, 389–393.

42. Zhu, L.J., Gazin, C., Lawson, N.D., Pagès, H., Lin, S.M., Lapointe, D.S., and Green, M.R. (2010). ChIPpeakAnno: a bioconductor package to annotate ChIP-seq and ChIP-chip data. BMC Bioinf. *11*, 237.

43. Yu, G., Wang, L.G., and He, Q.Y. (2015). ChIPseeker: an R/Bioconductor package for ChIP peak annotation, comparison and visualization. Bioinformatics *31*, 2382–2383.

44. Heinz, S., Benner, C., Spann, N., Bertolino, E., Lin, Y.C., Laslo, P., Cheng, J.X., Murre, C., Singh, H., and Glass, C.K. (2010). Simple combinations of lineage-determining transcription factors prime cis-regulatory elements required for macrophage and B cell identities. Mol. Cell *38*, 576–589.

45. Dobin, A., Davis, C.A., Schlesinger, F., Drenkow, J., Zaleski, C., Jha, S., Batut, P., Chaisson, M., and Gingeras, T.R. (2013). STAR: ultrafast universal RNA-seq aligner. Bioinformatics *29*, 15–21.

46. Ritchie, M.E., Phipson, B., Wu, D., Hu, Y., Law, C.W., Shi, W., and Smyth, G.K. (2015). Limma powers differential expression analyses for RNA-sequencing and microarray studies. Nucleic Acids Res. *43*, e47.

47. Robinson, M.D., McCarthy, D.J., and Smyth, G.K. (2010). edgeR: a Bioconductor package for differential expression analysis of digital gene expression data. Bioinformatics *26*, 139–140.

48. Yu, G., Wang, L.G., Han, Y., and He, Q.Y. (2012). clusterProfiler: an R package for comparing biological themes among gene clusters. OMICS *16*, 284–287.

49. Zhang, Z., Hernandez, K., Savage, J., Li, S., Miller, D., Agrawal, S., Ortuno, F., Staudt, L.M., Heath, A., and Grossman, R.L. (2021). Uniform genomic data analysis in the NCI genomic data commons. Nat. Commun. *12*, 1226.

50. Amemiya, H.M., Kundaje, A., and Boyle, A.P. (2019). The ENCODE blacklist: identification of problematic regions of the genome. Sci. Rep. *9*, 9354.

51. Law, C.W., Chen, Y., Shi, W., and Smyth, G.K. (2014). voom: precision weights unlock linear model analysis tools for RNA-seq read counts. Genome Biol. *15*, R29.

52. Chen, Y., Lun, A.T.L., and Smyth, G.K. (2016). From reads to genes to pathways: differential expression analysis of RNA-Seq experiments using Rsubread and the edgeR quasi-likelihood pipeline. F1000Res. *5*, 1438.

53. Patro, R., Duggal, G., Love, M.I., Irizarry, R.A., and Kingsford, C. (2017). Salmon provides fast and bias-aware quantification of transcript expression. Nat. Methods *14*, 417–419.

54. Soneson, C., Love, M.I., and Robinson, M.D. (2015). Differential analyses for RNA-seq: transcript-level estimates improve gene-level inferences. F1000Res. *4*, 1521.

STAR★METHODS

KEY RESOURCES TABLE

REAGENT or RESOURCE	SOURCE	IDENTIFIER
Antibodies		
PGC1α	Millipore	ST1203; RRID:AB_10806332
PPARγ (ChIPseq, Western)	Cell Signaling Tech.	2435; RRID:AB_2166051
PPARα	Proteintech	15540-1-AP; RRID:AB_2252506
HA tag (ChIPseq, IHC, Western)	Cell Signaling Tech.	3724; RRID:AB_1549585
HA tag (IHC)	Millipore Sigma	11867423001; RRID:AB_390918
HA tag (IHC, Western)	Novus	MAB0601
Actin	Sigma	A4700; RRID:AB_476730
ERRα	Abcam	Ab76228; RRID:AB_1523580
Hsp90	Santa Cruz Biotech	sc13119; RRID:AB_675659
C/EBPα	Cell Signaling Tech.	8178; RRID:AB_11178517
C/EBPβ	Boster	M01100
NCOA1	Cell Signaling Tech.	2191; RRID:AB_2196189
H3K27Ac (ChIPseq)	Cell Signaling Tech.	8173; RRID:AB_10949503
Chemicals, peptides, and recombinant proteins		
HBSS	Sigma	H1387-10X1L
16% Formaldehyde Solution	ThermoFisher Scientific	28906
DSG	Santa Cruz Biotech	sc-285455A
DSP	ThermoFisher Scientific	22585
Protein A magnetic beads	ThermoFisher Scientific	10001D
Protein G magnetic beads	ThermoFisher Scientific	10003D
RNAse A	Qiagen	19101
Protein K	ThermoFisher Scientific	EO0491
SuperScript™ VILO™ Master Mix	ThermoFisher Scientific	11755050
Critical commercial assays		
MinElute PCR Purification Kit	Qiagen	28004
PureLink™ RNA mini kit	ThermoFisher Scientific	12183018A
Deposited data		
ChIPseq and mRNAseq	GEO	GSE213601
Experimental models: Organisms/strains		
Mouse: B6;129-Txniptm1Rlee/J	The Jackson Laboratory	JAX: 016847
Mouse: B6.C-Tg(CMV-cre)1Cgn/J	The Jackson Laboratory	JAX: 006054
Mouse: B6.FVB-Tg(Adipoq-cre)1Evdr/J	The Jackson Laboratory	JAX: 028020
Mouse: BALB/cJ-Cebpbtm1.1Elgaz/J	The Jackson Laboratory	JAX: 032282
Software and algorithms		
Nikon Elements v.4.3	Nikon	https://www.microscope.healthcare.nikon.com/products/software/nis-elements
GraphPad Prism v9.1.1	GraphPad Software	
ImageJ software		https://imagej.nih.gov/ij/
TrimGalore v0.6.0		https://github.com/FelixKrueger/TrimGalore
bwa v0.7.17	(Li, 2013)[33]	

(*Continued on next page*)

Continued

REAGENT or RESOURCE	SOURCE	IDENTIFIER
SAMBLASTER v 0.1.24	(Faust and Hall, 2014)[34]	
SAMtools v1.9	(Li et al., 2009)[35]	
macs2 v2.2.7.1	(Zhang et al., 2008)[36]	
bedtools v2.29.2	(Quinlan and Hall, 2010)[37]	
deepTools v3.4.3	(Ramírez et al., 2016)[38]	
WiggleTools v1.2.11	(Zerbino et al., 2014)[39]	
wigToBigWig	(Kent et al., 2010)[40]	
DiffBind v3.2.7	(Ross-Innes et al., 2012)[41]	
ChIPpeakAnno v3.26.4	(Zhu et al., 2010)[42]	
ChIPseeker v1.28.3	(Yu et al., 2015)[43]	
HOMER v4.11.1	(Heinz et al., 2010)[44]	
STAR v2.7.8a	(Dobin et al., 2013)[45]	
Limma v3.48.3	(Ritchie et al., 2015)[46]	
edgeR v3.34.0	(Robinson et al., 2010)[47]	
clusterProfiler v4.0.2	(Yu et al., 2012)[48]	

RESOURCE AVAILABILITY

Lead contact

Further information and requests for resources and reagents should be directed to and will be fulfilled by the lead contact Ning Wu (ning@omnispacemail.com).

Materials availability

The KI mouse lines generated by this study will be available from JAX.

Data and code availability

ChIPseq and mRNAseq data generated during this study are available at GEO with accession number GSE213601.

No new code was generated.

No other new reagent was generated.

Any additional information required to reanalyze the data reported in this paper is available from the lead contact upon request.

EXPERIMENTAL MODEL AND SUBJECT DETAILS

Mice were maintained in a barrier facility, in accord with the Institute's regulations for animal care and handling (IACUC 21-04-012). Regular chow Labdiet 5010 (calorie composition: 28.7% from protein, 12.7% from fat, and 58.2% from carbohydrate) was used unless stated otherwise. Strains *Txnip* flox/flox (JAX 016847), CMV-Cre (JAX 006054), *Cebpb* flox/flox (JAX 032282) and Adipoq-Cre (JAX 028020) were purchased from the Jackson Laboratory. The total KO (CMV-Cre) mice were generated by crossing *Txnip* flox/flox with CMV-cre mice. The Cre transgene was bred out during the process. The mice were back-crossed to C57B6/J (JAX 000664) for over 10 generations.

For experiments, sex-matched littermates between 2 and 3 months old were used. To cold-shock the mice, each mouse was placed in a paper bucket with some food, but no bedding, and then was placed in the cold room for the indicated length of time (typically from 9 a.m. to 1 p.m.) before sacrifice by cervical dislocation.

The ketogenic diet was obtained from Envigo (TD.96355, calorie composition: 9.2% from protein, 90.5% from fat, and 0.3% from carbohydrate) and feeding was carried out as before.[6] Rosiglitazone-containing

diet was custom made with Envigo by including 36mg of rosiglitazone per kg of LabDiet 5010 (TD.210378, calorie composition: 28.7% from protein, 12.7% from fat, and 58.2% from carbohydrate). The mice were kept ad lib. on this diet for 2 weeks starting at 8–10 weeks of age.

METHOD DETAILS

Tagged knock-in mice construction

CRISPR component design, procurement and injection were performed by the VAI transgenic core. Sequence information for the target locus was downloaded from Ensembl.org. The 40 bp surrounding the KI integration point were analyzed for CRISPR guide sequences using crispor.tefor.net and deephf.com/#/cas9. Guide selection was based on proximity to the integration point, predicted cutting ability and specificity score (Table S3). The repair template consisted of the knock-in tag sequence with 60-70 bp arms of homology on either side, which was ordered as a single-stranded ultramer from IDT (Table S3). Guides were ordered as crRNA from IDT along with tracrRNA and Alt-R® S.p. Cas9 nuclease V3 protein. Upon arrival, the template and guide components were resuspended to 1 μg/μl in 0.02 μm filtered IDTE before storage at −80°C. The Cas9 protein was stored undiluted at −20°C. Complete CRISPR mix was prepared the morning of injection. Equimolar amounts of crRNA and tracrRNA were duplexed in a thermocycler by first heating to 95°C, then cooling to 25°C over the course of ~20 minutes. Cas9 protein was diluted to 2 μg/μl in 0.02 μm filtered IDTE, then added to the duplexed guides and left at room temperature for 10 minutes to allow protein:guide complexes to form. Temp late molecule was then added to yield an injection solution of final concentration 15 ng/μl duplexed guides, Cas9 protein and ultramer repair template in 0.02 μm filtered IDTE. Founder mice were screened by genotyping (Table S4) and sequencing. Mice were backcrossed to C57B6/J for at least 5 generations before used for experiments.

Western blots

Mice were sacrificed by cervical dislocation and intrascapular BAT was dissected out and frozen immediately in liquid nitrogen and stored at −80°C. Frozen tissues were lysed in RIPA buffer (30 mM Tris7.5, 120 mM NaCl, 1 mM vanadate, 20 mM NaF, 1% NP40, 1% deoxycholate, 0.1% SDS), plus protease inhibitors and calyculin A. The supernatant was used for running Western blots.

Histology

Tissue was fixed with 4% formaldehyde in PBS for 48h and sent to VAI histology core for embedding. Deparaffinization and antigen retrieval performed on Dako PT link platform using Dako High pH retriever buffer for 20 minutes at 97 degrees C. Staining performed utilizing Dako Autostainer Link 48, utilizing Dako Rabbit Polymer HRP for secondary for 20 minutes following primary antibody incubation for 30 minutes. DAB detection performed using Dako EnVision Flex Chromagen for 10 minutes and Dako Flex Hematoxylin for 5 minutes. Aperio scanning of slides was performed utilizing Leica Aperio AT2 system.

ImageJ software (NIH, Bethesda, MD) was used to quantitate the number of nuclei that were stained in each experimental condition. Positively stained nuclei were divided by the total number of nuclei to yield the percent of positive nuclei in BAT.

ChIP-seq

After treatment, BAT tissue was dissected out, minced in fixative buffer (HBSS pH 7.5, 2 mM DSG (disuccinimidyl glutarate) and fixed with rotation for 25 min at RT. Then formaldehyde was added to a final 0.8% concentration and the tissue pieces were further fixed for 12 min at RT. The reaction was terminated with addition of Tris 7.5 buffer (final 320 mM). The tissue pieces were spun down and washed one time with 50 mM Tris 7.5, 150 mM NaCl, frozen in liquid nitrogen and stored in −80°C for later processing.

Frozen tissue was mechanically lysed using an electric tissue homogenizer in 50 mM Tris 8.0, 2 mM EDTA. SDS was added to a final 1% concentration. The lysate was rotated at 4°C for 15 min, then sonicated using Diagenode Bioruptor UCD-200, 5″ on and 5″ off, for 3 cycles of 3 min on low setting. The sonicated lysate was cleared with a maximum speed spin in a cold bench top centrifuge for 10 min. The clarified lysate was diluted 10 times with ChIP wash buffer 1 (25 mM Tris 7.5, 5 mM $MgSO_4$, 100 mM KCl, 10% glycerol, and 0.1% NP40). The potassium-SDS precipitate was spun out at 4000g for 10 min. 1% of the lysate was saved as input before antibodies were added for binding overnight at 4°C. The next day, 1:1 mixture of protein A and protein G Dynabeads were added for 2 h. Then the beads were washed 3 times with ChIP wash buffer 1, 1 time

with ChIP wash buffer 2 (25 mM Tris 7.5, 5 mM $MgSO_4$, 300 mM KCl, 10% glycerol, and 0.1% NP40) and 3 times with (10 mM Tris 8.0, 1mM EDTA) before eluted with 30 mM Tris 7.5, 1% SDS. NaCl was added to the ChIP samples and input samples to a final 0.6 M concentration, and un-crosslinking was carried out in a 65°C water bath overnight. The next day, 1 μl RNAse A was added to each sample and sample was incubated at 57°C for 45 min, followed by incubation with proteinase K at 65°C for 45 min. The final DNA was purified with the Qiagen MinElute PCR purification kit and submitted to the VAI genomics core for library construction and sequencing.

Libraries for input and immunoprecipitated samples were prepared by the Van Andel Genomics Core from 10 ng of input material and all available IP material using the KAPA Hyper Prep Kit (v5.16) (Kapa Biosystems, Wilmington, MA USA). Prior to PCR amplification, end repaired and A-tailed DNA fragments were ligated to uniquely barcoded dual indexes (IDT, Coralville, IA USA). Quality and quantity of the finished libraries were assessed using a combination of Agilent DNA High Sensitivity chip (Agilent Technologies, Inc.), QuantiFluor® dsDNA System (Promega Corp., Madison, WI, USA), and Kapa Illumina Library Quantification qPCR assays (Kapa Biosystems). 50 bp, paired-end end sequencing was performed on an NovaSeq6000 sequencer using an S2, 100 bp sequencing kit (Illumina Inc., San Diego, CA, USA). Inputs were sequenced to a minimum of 60M reads and IPs to a minimum of 40M reads. Base calling was done Illumina RTA3 and output of NCS was demultiplexed and converted to FastQ format with Illumina Bcl2fastq v1.9.0.

Immunoprecipitation

BAT tissue was minced in buffer (HBSS pH7.5, 2 mM DSP (dithiobis(succinimidyl propionate))), crosslinked for 25 min at RT, and reactions stopped with Tris 7.5. The tissue was lysed with a combination of mechanical grinding and 1% NP40. The lysate was cleared with bench top centrifugation and protein A agarose beads were added for 1 h to pre-clear the mouse antibodies. Then antibodies were added for overnight IP at 4°C. The second day, protein A beads were added to precipitate the antibodies for 1 h. The beads were then washed 3 times with 50 mM Tris 7.5, 150 mM NaCl and 0.5% NP40 buffer. SDS-PAGE sample buffer with 50 mM DTT was added to the washed beads and samples heated at 100°C for 5 min to un-crosslink the complexes before running Western blots. Input samples were un-crosslinked the same way.

mRNAseq and qPCR

Total RNA was extracted with a PureLink RNA mini kit (Invitrogen12183018A) and submitted to the VAI genomics core. Libraries were prepared by the Van Andel Genomics Core from 500 ng of total RNA using the KAPA Stranded mRNA-Seq Kit (Roche). RNA was sheared to 200–300 bp. Prior to PCR amplification, cDNA fragments were ligated to Bioo Scientific NEXTflex DNA Barcodes (Bioo Scientific, Austin, TX, USA). The quality and quantity of the finished libraries were assessed using a combination of Agilent DNA High Sensitivity chip (Agilent Technologies, Inc.), QubitdsDNA HS Assay Kit (ThermoFisher Scientific, Waltham, MA), and Kapa Illumina Library Quantification qPCR assays (Kapa Biosystems). Individually indexed libraries were pooled and 75-bp, single-end sequencing was performed on an Illumina NextSeq 500 sequencer using a 75-bp HO sequencing kit (Illumina Inc., San Diego, CA, USA). Base calling was done by Illumina NextSeq Control Software (NCS) v2.0, and the output of NCS was demultiplexed and converted to FastQ format with Illumina Bcl2fastq v1.9.0.

For qPCR, total RNA was reverse-transcribed into cDNA using SuperScript IV Vilo Mastermix (Invitrogen). Primer sets used can be found in Table S5. For statistics, an unpaired Student's t-test was performed using GraphPad Prism version 8.00 for Windows, GraphPad Software, La Jolla California USA.

Bioinformatics: ChIP-seq analysis

Reads were trimmed using TrimGalore v0.6.0 (https://github.com/FelixKrueger/TrimGalore) with default settings. Trimmed reads were aligned to the GRCm38.p6 reference genome from GENCODE vM24 using bwa mem v0.7.17.[33] In the case of the C/EBPA and wildtype cold/RT H3K27ac datasets, the reference was concatenated with decoy sequences.[49] Duplicates were marked using SAMBLASTER v 0.1.24.[34] Alignments were filtered using SAMtools view v1.9[35] with the parameters '-q 30 -F 2828' and '-f 2' for paired-end reads. Peaks were called using macs2 v2.2.7.1[36] with the parameters '-g mm -q 0.05' and '-f BAMPE' for paired-end reads, using the corresponding input sample as the control. Peaks overlapping ENCODE blacklist v2 regions[50] were removed using bedtools v2.29.2.[37]

Bigwig files were generated using deepTools bamCoverage v3.4.3[38] with the parameters '–binSize 10 –normalizeUsing "CPM" –samFlagExclude 1024', specifying the ENCODE v2 blacklist using '–blackListFileName'; for paired-end reads, the parameters '–samFlagInclude 64 –extendReads' were added. Bigwig files of replicates were combined by computing the mean signal using WiggleTools v1.2.11[39] and converting back to Bigwig format using wigToBigWig.[40] Coverage profiles and heatmaps were created using the functions computeMatrix and plotHeatmap in deepTools v3.4.3.

Differential binding was tested using DiffBind v3.2.7.[41] The parameter 'bUseSummarizeOverlaps = TRUE' was used with dba.count and the parameters 'normalize = DBA_NORM_NATIVE, background = TRUE' were used with dba.normalize. An adjusted P-value cutoff of 0.05 was used. Peak overlap Venn diagrams were created using the 'makeVennDiagram' function from ChIPpeakAnno v3.26.4.[42] For summarized visualizations, peaksets were merged across replicates. Peaks were annotated to their nearest genes using the annotatePeak function in ChIPseeker v1.28.3;[43] for the PGC1A peaks, 'tssRegion=c(-3000, 500)' was used. Enriched motif were identified using the 'findMotifsGenome.pl' script from HOMER v4.11.1[44] with the preset 'mm10' genome and the parameter, '-size given'.

Bioinformatics: RNA-seq analysis

Reads were trimmed using TrimGalore v0.6.0 (https://github.com/FelixKrueger/TrimGalore) with default settings. Using STAR v2.7.8a,[45] trimmed reads were aligned to the GRCm38.p6 reference genome from GENCODE vM24 and gene counts were obtained. Differential expression analysis of the dataset containing the *txnip* KO was done using the limma-voom (limma v3.48.3) workflow.[46,51] A design of '~0 + Group' was fitted, where 'Group' was the combination of genotype (wildtype or knock-out) and temperature (RT or cold-treated), and littermate information was incorporated using the 'duplicateCorrelation' function.

Differential expression analysis of the dataset containing the *cebpb* AKO$^{\beta}$ was done using the quasi-likelihood workflow in edgeR v3.34.0.[47,52] Separate models were fitted for each pairwise contrast, incorporating the litter information where the litters were not redundant with the groups being compared. Significant genes were identified using an adjusted P-value cutoff of 0.05. GSEA was conducted using clusterProfiler v4.0.2,[48] ranking based on the -log10(P-value) multiplied by the sign of the log fold change. MSigDB genesets were retrieved using misgdbr v7.4.1.

To calculate transcripts per million (TPM) values, Salmon v1.5.2[53] was used. The index was constructed using Gencode vM24 transcripts, specifying the genome chromosomes/contigs as decoys using the '-d' parameter in the 'salmon index' command. Expression values were calculated using the 'salmon quant' command with the parameters '-l A –validateMappings'. Finally, per-gene TPMs were calculated using the R package, tximport v1.20.[54]

QUANTIFICATION AND STATISTICAL ANALYSIS

Unless stated otherwise in the method details section, we assumed a normal distribution of the samples and unpaired, two tailed student's t-test was used (GraphPad Prism) for pairwise comparisons and ordinary one-way ANOVA multiple comparisons test for more than 2 groups (GraphPad Prism). The numbers of animals used (n), mean values and standard deviations were reported in figures.